ARL-TR-10451 • Sep 2026

Integrated Photonic Reflection Controlling Circuit for Attached Laser Stabilization

by Valerie J. Yoshioka, Pak S. Cho, and Justin R. Bickford

NOTICES

Disclaimers

ARL-TR-10451 ● SEP 2026

Integrated Photonic Reflection Controlling Circuit for Attached Laser Stabilization

Valerie J. Yoshioka
Oak Ridge Associated Universities, Postdoctoral Fellowship

Pak S. Cho
General Technical Services

Justin R. Bickford
DEVCOM Army Research Laboratory

REPORT DOCUMENTATION PAGE

1. REPORT DATE	2. REPORT TYPE	3. DATES COVERED START DATE	END DATE
September 2026	Technical Report	2/1/2024	8/26/2026

4. TITLE AND SUBTITLE
Integrated Photonic Reflection Controlling Circuit for Attached Laser Stabilization

5a. CONTRACT NUMBER	5b. GRANT NUMBER	5c. PROGRAM ELEMENT NUMBER
W911NF-24-2-0212		
5d. PROJECT NUMBER	**5e. TASK NUMBER**	**5f. WORK UNIT NUMBER**

6. AUTHOR(S)
Valerie J. Yoshioka, Pak S. Cho, and Justin R. Bickford

7. PERFORMING ORGANIZATION NAME(S) AND ADDRESS(ES)
DEVCOM Army Research Laboratory
ATTN: FCDD-RLA-P
Adelphi, MD 20783

8. PERFORMING ORGANIZATION REPORT NUMBER
ARL-TR-10451

9. SPONSORING/MONITORING AGENCY NAME(S) AND ADDRESS(ES)	10. SPONSOR/MONITOR'S ACRONYM(S)	11. SPONSOR/MONITOR'S REPORT NUMBER(S)

12. DISTRIBUTION/AVAILABILITY STATEMENT
DISTRIBUTION STATEMENT A. Approved for public release: distribution unlimited.

13. SUPPLEMENTARY NOTES
ORCID: Valerie J. Yoshioka, 0000-0001-5777-1090

14. ABSTRACT
To achieve stable laser operation in a photonic integrated circuit (PIC) system, we implemented an on-chip reflection controlling circuit (RCC), which controls the phase and amplitude of reflections from the on-chip system back into the laser. By adjusting the phase of the back-reflected light, we can prevent or induce instability in laser operation at a given operation point using on-chip controls rather than external isolation. In this work, we characterize the stability of a distributed feedback laser diode at 1550 nm that is photonically wire bonded to an on-chip PIC system. Although internal losses in the PIC system were sufficiently high to prevent measurable laser instability from intrinsic back reflections, we used the RCC to force the laser between stable and unstable modes of operation, demonstrating its utility in controlling laser dynamics. As system losses improve in future iterations of our PIC devices, intrinsic back reflections have the potential to induce instability, necessitating on-chip control methods to stabilize lasing.

15. SUBJECT TERMS
integrated photonics; laser attachment; photonic wire bond; laser stabilization; Advanced Photonics, Electronics, and Quantum Sciences

16. SECURITY CLASSIFICATION OF: a. REPORT	b. ABSTRACT	C. THIS PAGE	17. LIMITATION OF ABSTRACT	18. NUMBER OF PAGES
UNCLASSIFIED	UNCLASSIFIED	UNCLASSIFIED	UU	34

19a. NAME OF RESPONSIBLE PERSON	19b. PHONE NUMBER *(Include area code)*
Valerie J. Yoshioka	(520) 851-0660

STANDARD FORM 298 (REV. 5/2020)
Prescribed by ANSI Std. Z39.18

Contents

List of Figures

Acknowledgments

The authors thank Dream Photonics for their discussions on design, laser stabilization, and fabricating the photonic wire bonds for our devices. Fabrication of the photonic chips was performed by AIM Photonics Foundry Services.

Valerie J. Yoshioka acknowledges support from Oak Ridge Associated Universities Postdoctoral Fellowship. Research was sponsored by ARL and was accomplished under Cooperative Agreement Number W911NF-24-2-0212.

1. Introduction

Lasers are susceptible to instability induced by parasitic back reflections. Bulk laser systems mitigate these reflections using free-space isolators, which traditionally use magneto-optic effects to break reciprocity. Although on-chip isolators can also use magneto-optic effects to achieve nonreciprocal operation, they require heterogeneous integration of magneto-optic materials and a magnetic field source, whether external or integrated as an electromagnet.[1] Alternate methods to break reciprocity have also been explored. Spatiotemporal modulation[2] has been used but requires higher power to drive complex modulation schemes. Nonlinear optical effects[3] provide a purely passive method but often require strong optical power to function. Self-injection locking[4] provides linewidth reduction in addition to stabilization but requires aligning the laser frequency to the external cavity resonance, potentially increasing system loss. superfluous

In this work, we implement a frequency-agnostic, tunable reflection controlling circuit (RCC), as demonstrated by Esmaeeli et al.,[5] to control laser dynamics in our photonic integrated circuit (PIC) systems. Since it can be fabricated in the same silicon photonics process as the rest of our system, fabrication complexity is greatly reduced, enabling scalable production. Its lack of frequency-dependent resonances makes it widely usable without the need to control the laser wavelength to achieve a stable lasing state. Its simplicity and small footprint make it a viable candidate for compact, fully integrated devices. Although the concept has been proven in other foundry processes,[5] we designed and fabricated the silicon photonic chip using the AIM Photonics foundry process with our internally designed components to explore its functionality in our custom devices.

2. Circuit Layout

On the input side, the distributed feedback (DFB) laser was photonically wire bonded to an edge coupler (EC) to couple light into the chip. The major elements of the RCC are a tunable Mach-Zehnder interferometer (MZI) and loop mirror (Figure 1). The MZI is used to selectively direct power to the output port or to the loop mirror. By changing this ratio, the amplitude of back-reflected optical power can be adjusted. An additional heater before the loop mirror is used to adjust the phase of the back-reflected light. By adjusting both of these parameters, laser stability can be achieved. In our device, we also included a directional coupler (DC) at the output port to direct light to an on-chip photodetector (PD) for power and stability monitoring and an on-chip PIC system. In this work, the PIC system was designed for free-space optical communication, but a variety of applications could also be implemented. An additional PD on the fourth port of the DC can be used to monitor intrinsic back reflections from the on-chip structures downstream. We also implemented doped silicon blocks adjacent to the waveguide to absorb unintended higher-order modes (HOMs) without inducing further loss to the fundamental mode.[6]

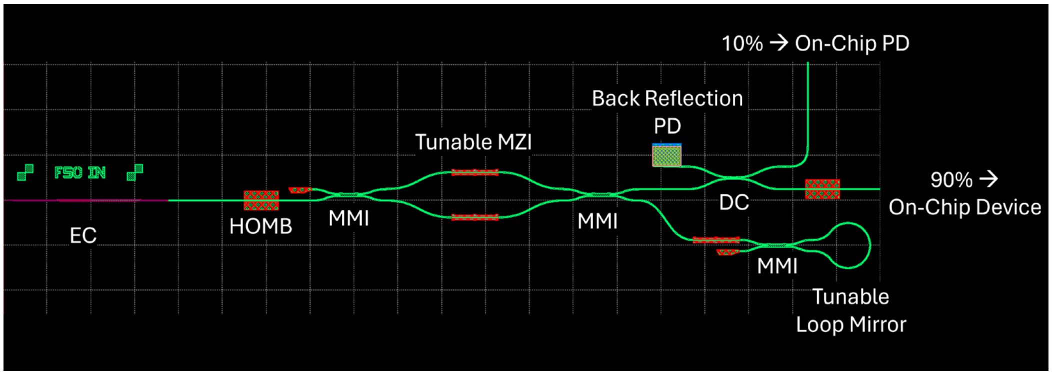

Figure 1. RCC with labeled components: EC, HOM blocks (HOMBs), tunable MZI with 2 × 2 multi-mode interferometers (MMIs) and heaters, tunable loop mirror, and a 90:10 DC to direct light to an on-chip PD and on-chip system. A back reflection PD is used to monitor any parasitic reflections from on-chip components.

3. Components

Because many of the components in this circuit were internally designed, we provide characterization data for each component in the circuit to fully predict the device performance. All components are designed for the fundamental TE0 mode at 1550 nm on the silicon-on-insulator platform provided by AIM Photonics.

3.1 Waveguides

The routing waveguides are designed to be 480-nm width, 220-nm height crystalline silicon waveguides in oxide cladding. Based on spiral propagation loss structures on the same wafer, the loss is estimated to vary from −1.65 to −2.2 dB/cm between chips. The orientation of the waveguides and the wavelength have minimal effect on loss (Figure 2). The spiral structure with vertical waveguides exhibits slightly higher losses at approximately −2.25 dB/cm, rather than −1.8 dB/cm for the spiral with horizontal waveguides, but the difference over small lengths is minimal. The bends in the spirals used a radius of 10 μm, so bend loss is expected to be negligible.

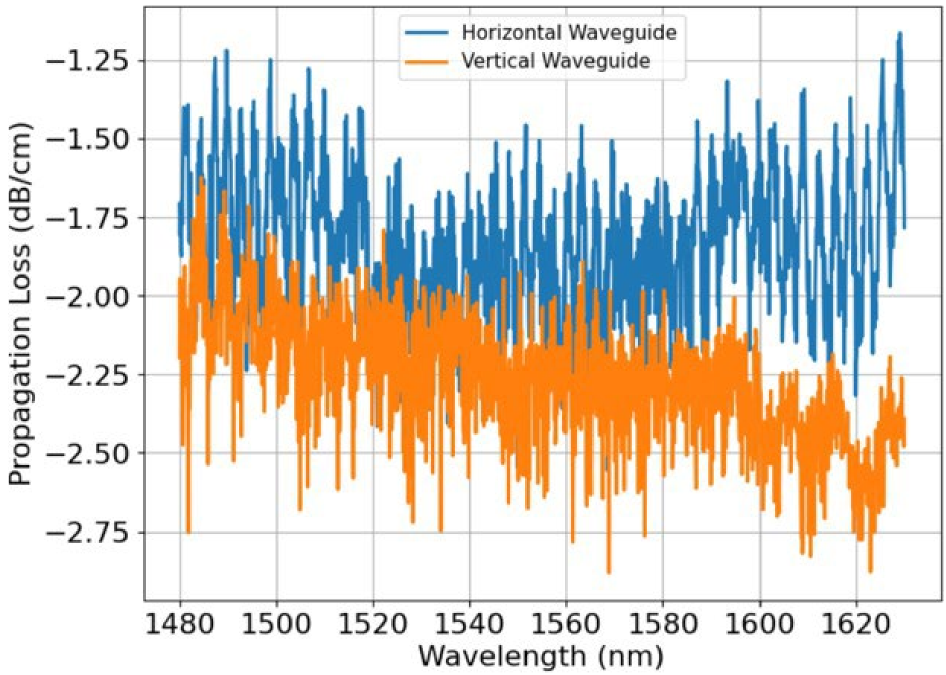

Figure 2. Propagation loss vs. wavelength for horizontal and vertical waveguide spiral structures, with an average of 2 ± 0.5 dB/cm. Wavelength has a minor effect on loss.

3.2 Edge Coupler

The EC escalates light from the silicon waveguide to a silicon nitride layer, and then to a second nitride layer above the first, at which point it exits the side of the chip. The narrow width of the final nitride taper at the chip edge forces the light to be poorly confined and have a larger mode field diameter (MFD) that better matches the intended output mode for 1) lensed or cleaved fiber coupling or 2) photonic wire bonds (PWBs). For this coupler, the simulated output MFD in air is approximately 4 µm (Figure 3). However, since the output facet of the EC is rectangular, the free-space mode field deviates from a Gaussian beam, so there is some coupling loss from imperfect mode overlap. When coupling light into the chip, increasing the MFD of the input beam from air achieves stronger coupling, with a 5-µm MFD corresponding to a transmission insertion loss of −1.92 dB (Figure 4).

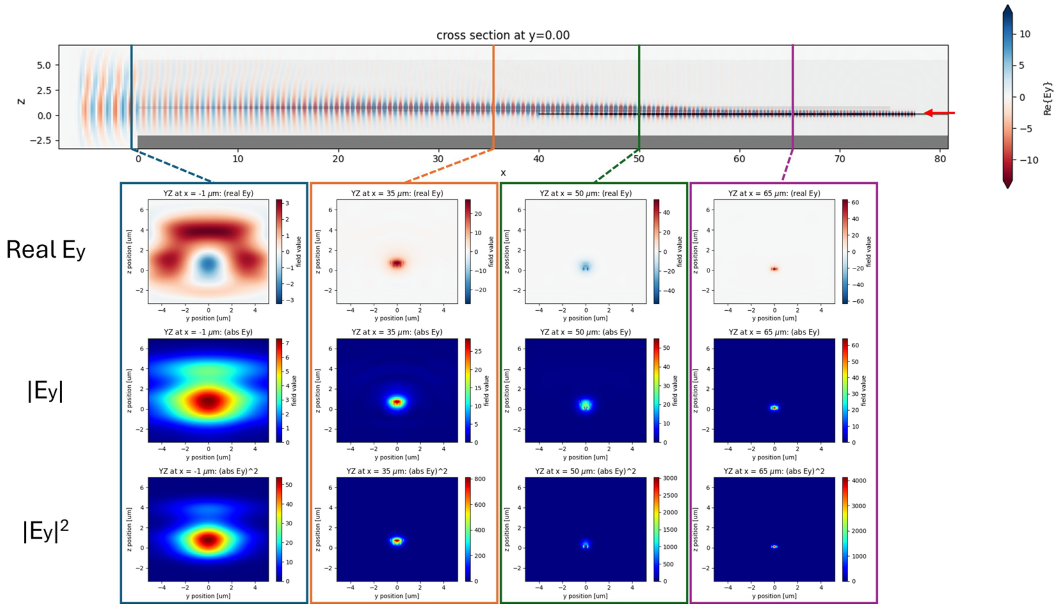

Figure 3. **Simulated waveguide mode evolution along the EC for E_y, the dominant component in the TE0 mode. Light is injected into the silicon waveguide from the right side (red arrow) and travels in silicon (purple box) before coupling into the first nitride layer (green box). The mode continues to spread in the second nitride layer (orange box) before finally exiting into free space with an expanded MFD (blue box).**

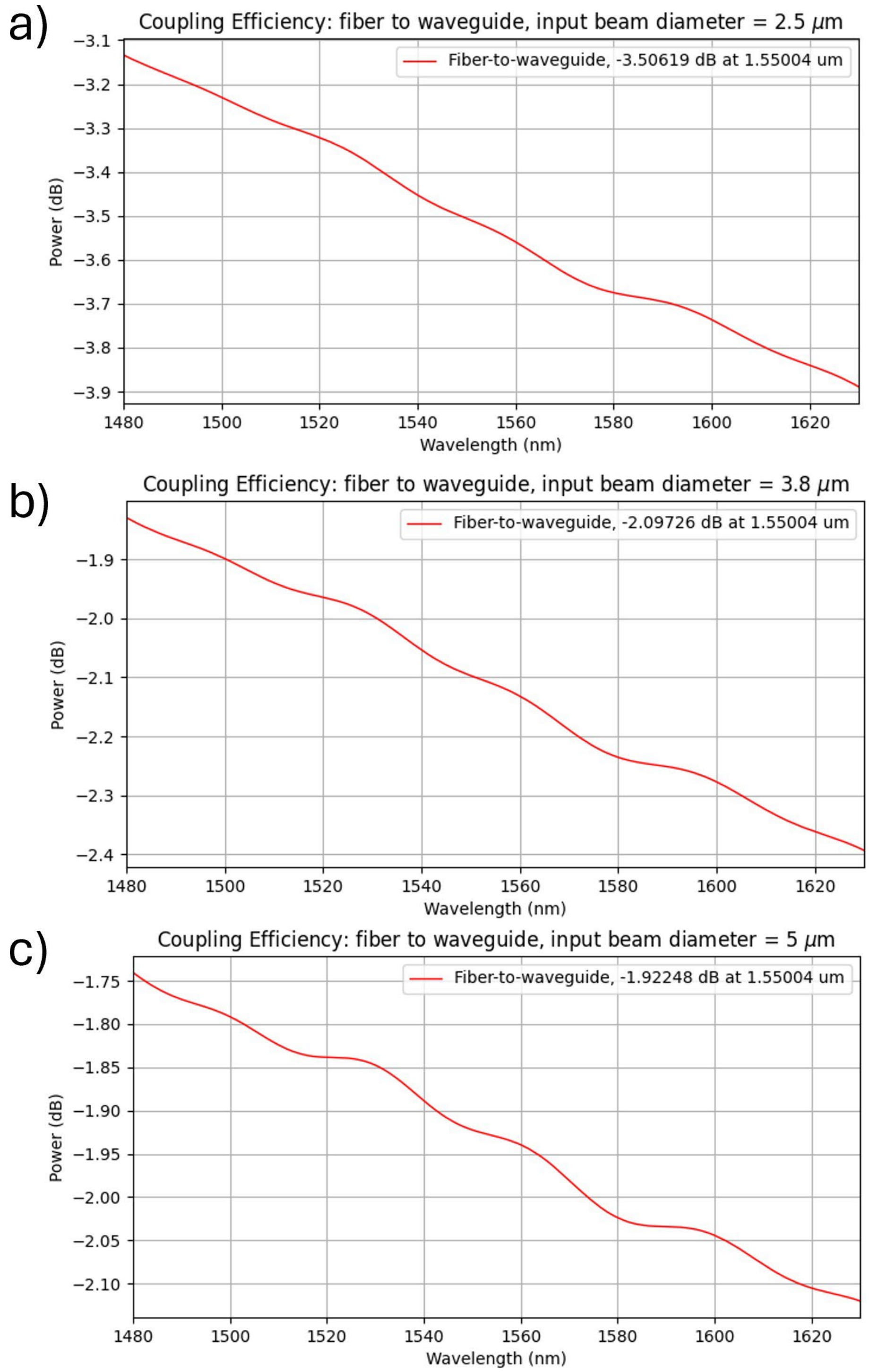

Figure 4. Simulated coupling efficiency vs. wavelength between a free-space Gaussian beam in air and EC with input free-space MFDs of a) 2.5 µm, b) 3.8 µm, and c) 5 µm.

3.3 Heater

To control phase in the tunable MZI and loop mirror, we used thermo-optic phase shifters formed from doped silicon segments with electrical contacts placed in proximity to a waveguide. By applying a voltage, current flows through the doped silicon, which acts as a resistor and generates heat. The partial-height heaters include an additional contact between doped silicon and metal to reduce resistance and thus the voltage required to achieve high power. Heaters are included on either side of the waveguide for higher efficiency. The phase shift scales linearly with applied power, so the MZI transmission versus power exhibits the expected sinusoidal behavior (Figure 5b). Since heater resistance changes with applied voltage, the transmission versus voltage deviates from sinusoidal (Figure 5a). Since V_π is approximately 4.3 V (Figure 5), microcontrollers with a 5V output limit can be used to control these heaters up to a π phase shift for a compact electronic control system.

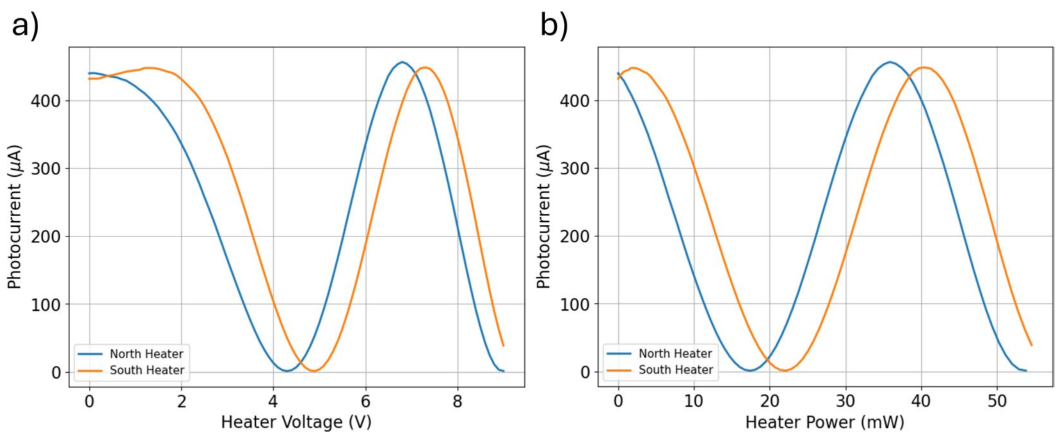

Figure 5. Thermo-optic phase shifter response in an MZI vs. a) voltage and b) power for partial-height heaters.

3.4 Directional Coupler

The DC is used to split light between an on-chip monitor PD and a functional, on-chip system. Light travels from the input port and either continues on the same path to the bar port toward the on-chip system or switches over to the cross port connected to an on-chip PD. The other input port is terminated by a PD to monitor back reflections. The splitting ratio has some dispersion over the wavelength region of interest, varying from 90:10 at 1480 nm to 78:22 at 1630 nm (Figure 6). At 1550 nm, the bar port transmission is 88.5% and the cross port is 11.5%.

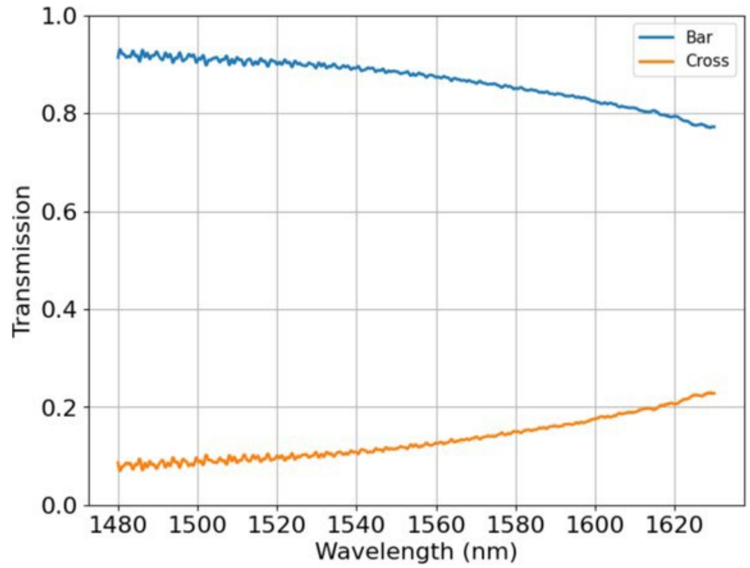

Figure 6. DC splitting ratio vs. wavelength. Most light is directed toward the bar port while 10%–20% is directed toward the opposite cross port.

3.5 Multi-Mode Interferometer

The MMI is used as a splitter and combiner to form the tunable MZI and loop mirror. According to simulations, the splitting ratio at 1550 nm is approximately 50:50, with losses below −0.3 dB (Figure 7). Although experimental data of the isolated component is unavailable, the simulated behavior matches its performance in systems. We use splitters with 2 input and 2 output ports, rather than 1 × 2, to avoid excitation of evanescent HOMs that result from combining out-of-phase signals. In 2 × 2 combiners, destructive interference couples light to the other output port, which can be terminated using absorptive highly doped silicon, whereas 1 × 2 combiners couple light into HOMs that can persist and affect system performance.

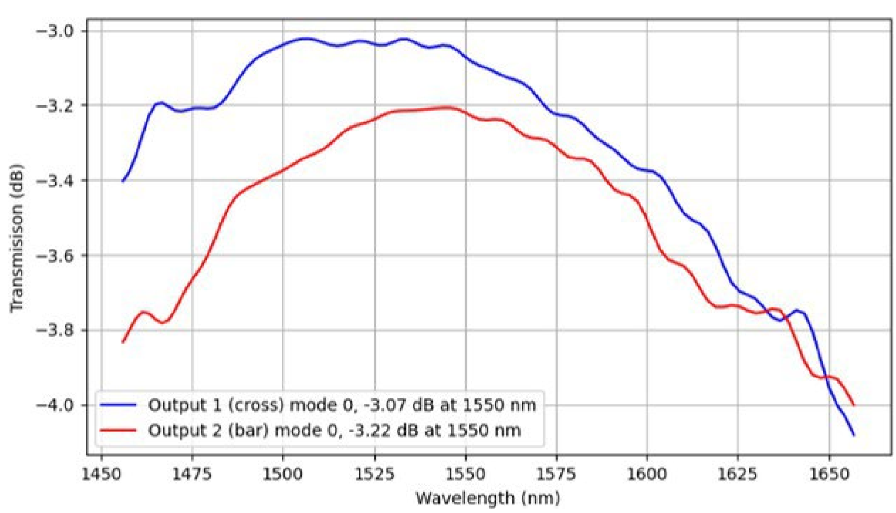

Figure 7. Simulated MMI transmission per output arm vs. wavelength.

3.6 Photodetector

The on-chip PDs utilize Ge-on-Si and couple light from the waveguide into the detector region via evanescent taper, improving coupling compared with alternative taper methods.[7,8] Based on a similar PD design fabricated through AIM Photonics,[8] responsivity is estimated to be 1 A/W at 1550 nm, with lower responsivity at longer wavelengths. Our PD has similar dispersion with additional ripples due to back reflections, which are attributed in some part to the uncoated chip facet (Figure 8). By comparing the strength of these ripples to the maximum photocurrent,[9] we estimate back reflections between the PD and edge facet to be −18 dB.

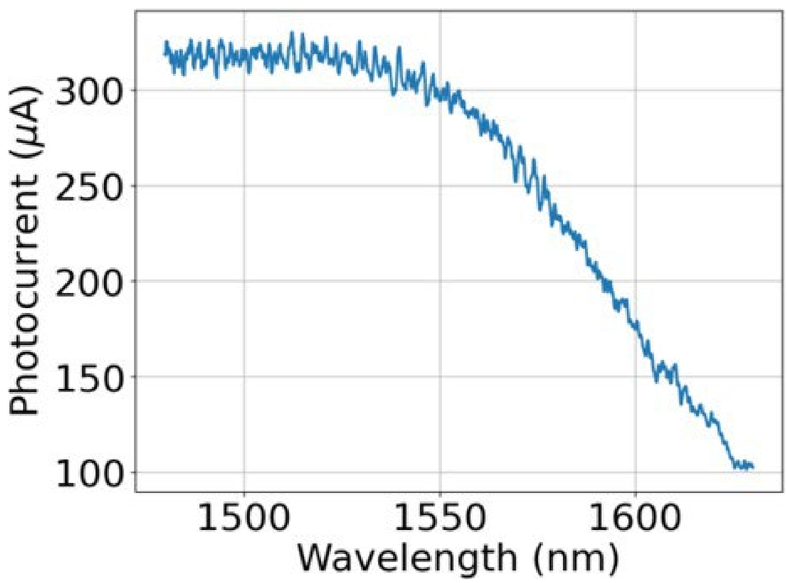

Figure 8. On-chip Ge-on-Si PD characterization. The measured response from 1480 to 1630 nm for our PD design has some wavelength dispersion, with higher responsivity at shorter wavelengths. Interference ripples are due to back reflections between the PD and edge facet.

3.7 HOM Attenuation

Although the components and layout of our on-chip circuit have been designed to prevent issues from HOM excitation, HOMs can still be generated by misaligned coupling, whether lateral or angular. To prevent their propagation within and past the circuit, we include HOM attenuators throughout. The HOMBs are highly doped silicon blocks adjacent to the waveguide. Based on prior measurements, these absorptive blocks can reduce HOMs by at least −10 dB, without adding significant loss to the fundamental mode.[6] For passive fabrication processes that do not allow doping or absorptive materials, tightly curved Z-bends, formed from two 90° Euler bends, can also be used to strip out HOMs while retaining power in the fundamental mode.

3.8 DFB Characterization

We used directly modulated DFB laser diode chips (model DFB-1550-B-B-CH5-B28) with anti-reflection coating from Applied Optoelectronics, Inc. (AOI; Sugar Land, Texas) for our measurements. The die used for the following measurements had reported room temperature specifications: side mode suppression ratio (SMSR) of 46.5 dB, wavelength of 1549.41 nm, efficiency of 0.295 mW/mA, and threshold of 4.75 mA. Measurements of a similar die, including optical spectrum analyzer (OSA) measurements (Figure 9), dependence on current (Figure 10), and dependence on temperature (Figure 11), indicated similar performance to these reported specifications.

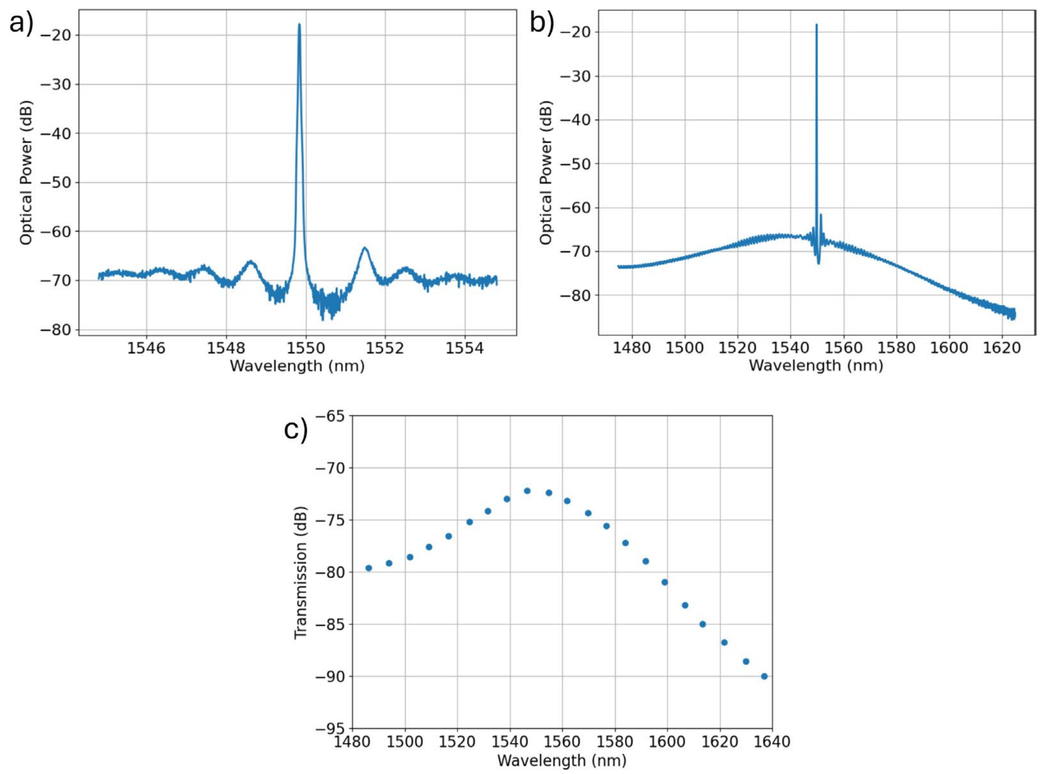

Figure 9. DFB spectral response at 25 °C with a DFB current of 10 mA. a) OSA spectra, with center wavelength of 1549.84 nm. The side peak is offset by 1.65 nm, with SMSR at approximately 45 dB. b) OSA spectra over a wide wavelength span, with center wavelength of 1549.84 nm. c) Gain spectrum. Maximum output power without lasing is −72.3 dB at 1549.55 nm, and the 3-dB bandwidth is 50.24 nm.

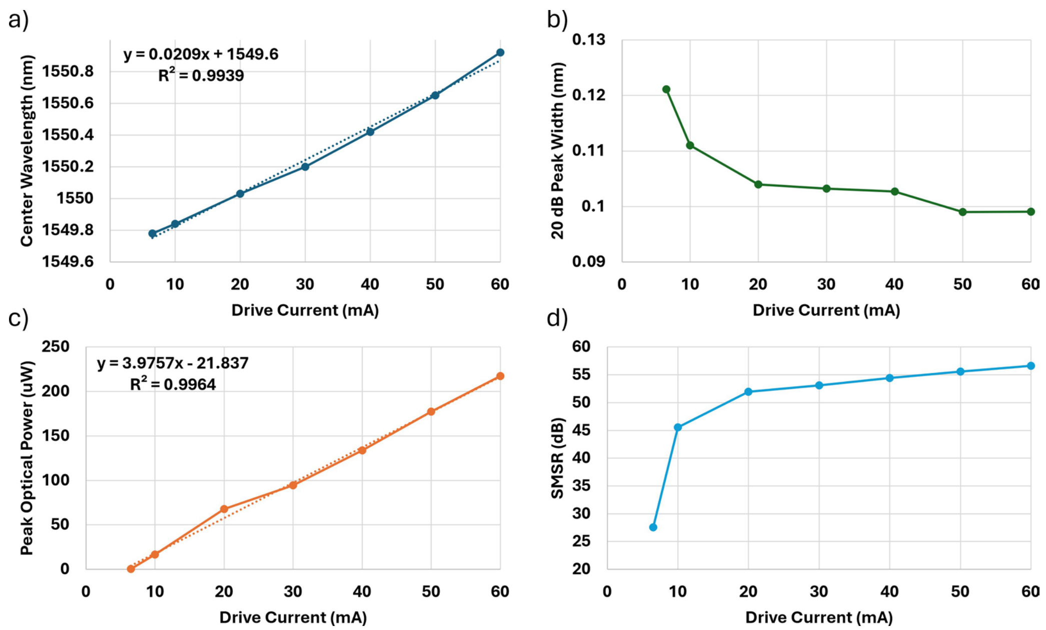

Figure 10. DFB performance vs. drive current at 25 °C. a) Center wavelength, b) 20-dB peak width, c) peak optical power, and d) SMSR vs. drive current.

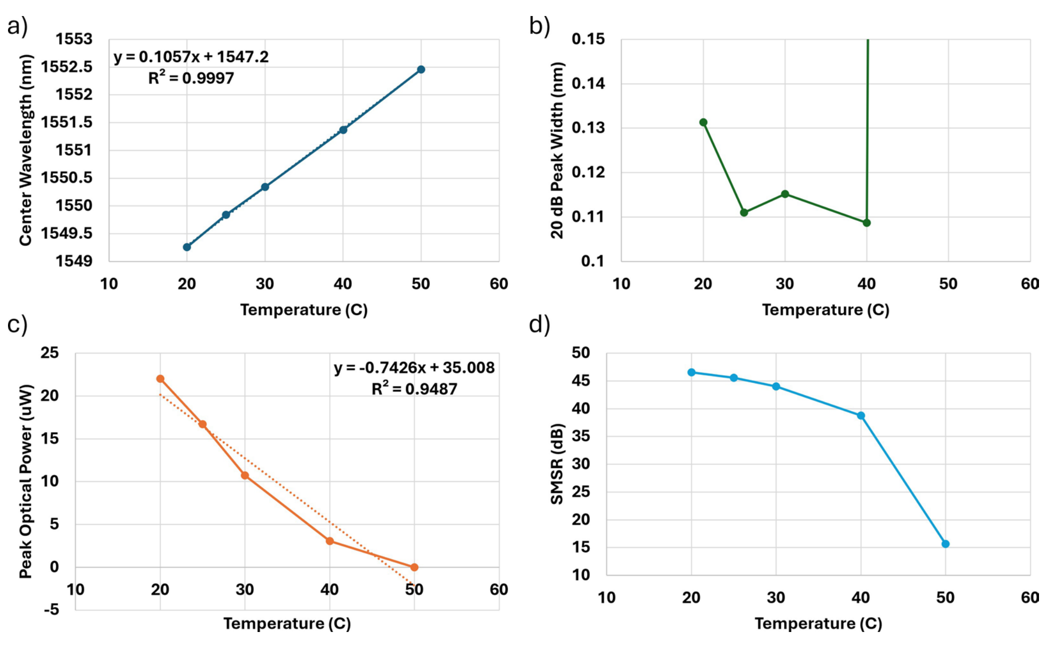

Figure 11. DFB performance vs. temperature at drive current of 10 mA. a) Center wavelength, b) 20-dB peak width, c) peak optical power, and d) SMSR vs. temperature.

3.9 Photonic Wire Bond

The PWB dimensions are elliptical, with the major axis oriented in the horizontal direction, to better match the elliptical output mode formed by the rectangular waveguide of the EC (Figure 3). In the middle of the bond, the width of the PWB is 2.2 µm and the height is 1.8 µm. To improve coupling between the PWB and chip, a 50-µm taper is used to gradually increase the core size of the PWB (Figure 12a). Based on simulations, the optimal core size at the interface of the chip is approximately 7.8 × 5.6 µm to maximize mode overlap to −1.3 dB (Figure 12b). Transmission between the EC and PWB is simulated to be −2.21 dB at 1550 nm (Figure 12c), with field simulations showing reasonable matching between the PWB and EC modes at the X = 0 µm position (Figure 12d). The dimensions for the PWB connection to the laser are approximately 3.5 × 3 µm at the attachment point, tapering to 2.2 × 1.8 µm over 40 µm. Based on simulations, the estimated laser-to-PWB loss is −1 dB. Thus, the expected total PWB loss is at least −3.21 dB. Optical images of the fabricated PWB indicate that the PWB is smooth and well anchored, with no obvious mechanical defects that would increase loss (Figure 13).

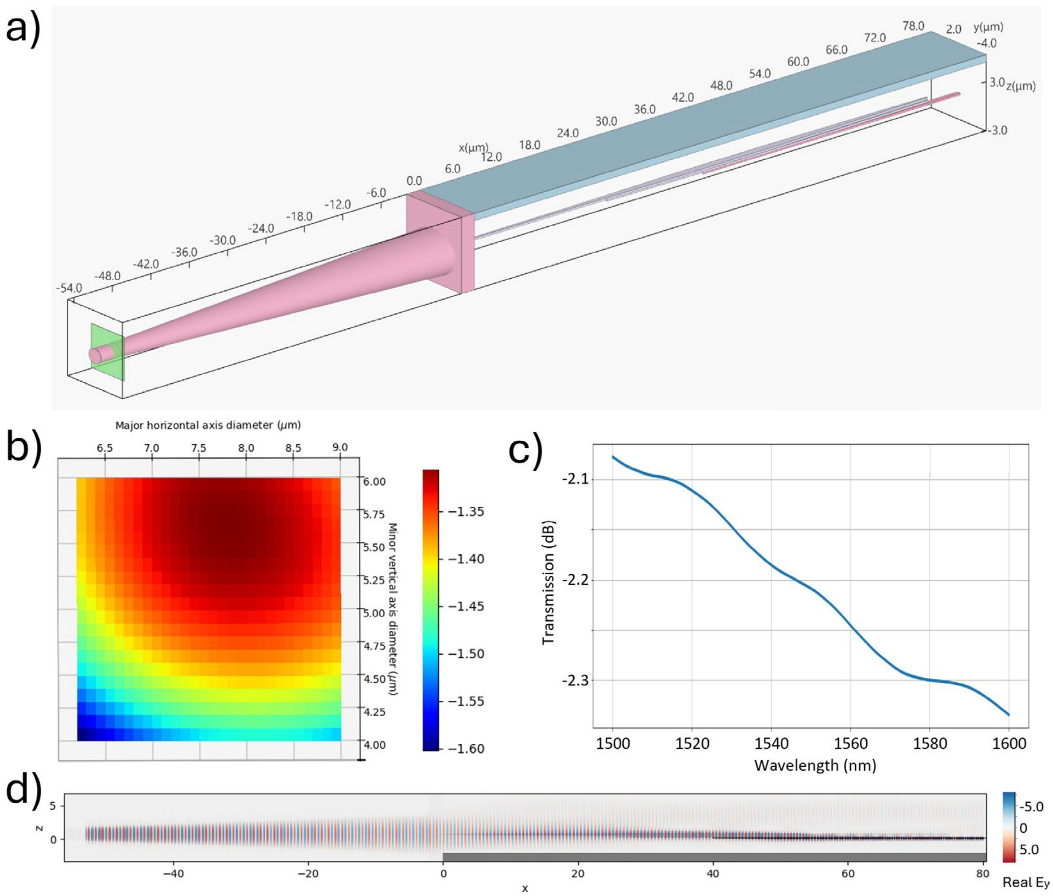

Figure 12. Simulated coupling efficiency between the center of the photonic wire bond and the EC. a) 3D geometry of PWB taper (pink), PWB cladding (blue), EC (gray), and silicon waveguide (pink). b) Mode overlap between PWB and EC at 1550 nm in dB vs. PWB core size. The optimal size is 7.8 × 5.6 µm, with a maximum overlap of −1.3 dB. c) Simulated transmission between a 50-µm-long PWB, tapering from a 2.2 × 1.8- to 7.8 × 5.6-µm core, and EC vs. wavelength. Transmission at 1550 nm is −2.21 dB. d) Real part of E_y at 1550 nm when light is coupled from the 50-µm-long PWB into the EC.

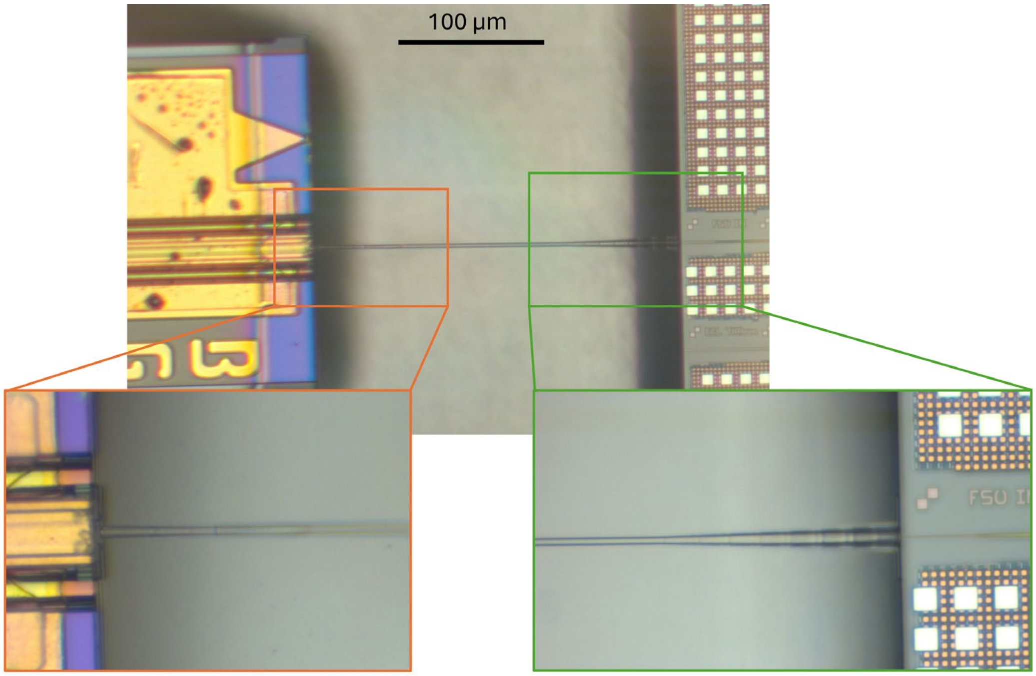

Figure 13. Microscope images of the photonic wire bond between the DFB laser and on-chip waveguide, with zoomed-in views of the attachment points to the laser and PIC.

4. Measurements

Laser performance and stability were characterized through a variety of measurements. Optical power and wavelength versus input parameters such as drive current and temperature provide information on the performance of the laser. Significant changes in optical power or the presence of side peaks in the optical spectrum indicate instability. By using a PD to monitor output power from an unstable laser, the resultant photocurrent includes noise at specific frequencies that can be observed by an RF spectrum analyzer or envelope detector.

4.1 Optical Power

The optical power versus drive current for the DFB when photonically wire bonded indicates reasonable performance (Figure 14). The measurements were performed at 25 °C, with both MZI and loop mirror heaters remaining unheated, directing almost all of the power toward the output rather than the loop mirror. The output optical power is measured by the on-chip PD. The expected threshold at room temperature is 4.75 mA, whereas our measurement at 25 °C indicates a similar threshold at approximately 5.75 mA. Mode hops occur at higher DFB currents, particularly around 90 mA, as evidenced by deviations in power from the linear trend. However, these mode hops do not significantly impact output power.

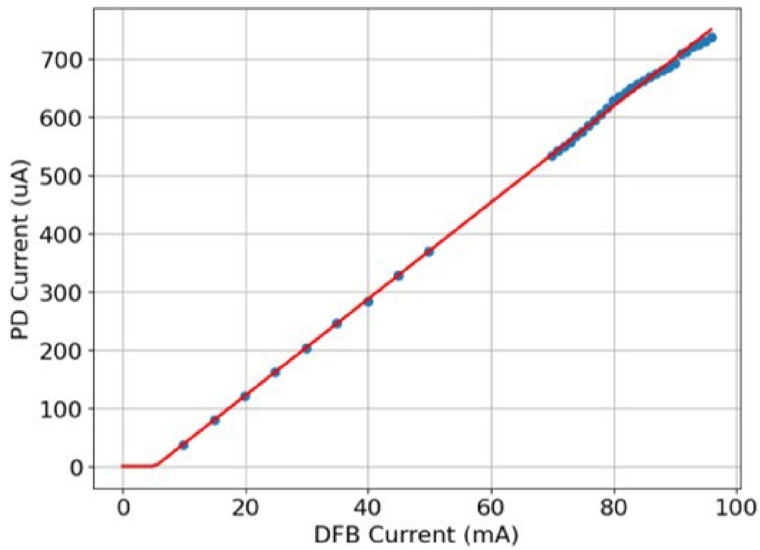

Figure 14. Optical power vs. drive current for the photonically wire-bonded DFB at 25 °C with unheated MZI and loop mirror. Threshold current is 5.75 mA. The linear fit for photocurrent I_{PD} in μA as a function of drive current I_0 in mA is $I_{PD} = 8.289 \times I_0 - 44.035$.

By tracking the increase in optical power as a function of drive current, it is possible to extract an estimate of PWB loss. The fitted slope is approximately 0.008 mW of optical power at the on-chip monitor PD per milliamp of drive current. The PD responsivity at 1550 nm is expected to be approximately 1 A/W based on reported values from similar on-chip PDs (Figure 8). The expected efficiency for this DFB is 0.295 mW/mA based on its provided specifications, indicating a total loss of −15.51 dB in the connected system. On-chip losses include the following: −9.39 dB loss due to the DC splitting ratio, −0.055 dB loss due to the MZI splitting ratio when unheated, −0.56 dB from a propagation loss of −2 dB/cm over 2.8 mm, and −0.29 dB additional loss from the MMIs based on simulated values; total on-chip losses sum to −10.295 dB. Thus, the additional loss of −5.215 dB is attributed to the PWB losses. Although the actual loss may be slightly better due to MMI behavior, variation in PD responsivity, and slight differences in measurement temperatures, the estimate is reasonable compared with the minimum value of 3.21 dB, which assumed perfect alignment, fabrication, and no bending in the PWB.

When the DFB drive current is tuned from 80 mA to 100 mA to 80 mA in time, we can observe whether the trend in output power remains linear to check whether the laser is operating in a stable state (Figure 15). When all the light is directed toward the output port, as is the case when the MZI and loop heaters are unbiased, the increase in optical power versus current remains monotonic. The power may not increase linearly with drive current for every small increment, but it follows the same trend. When 30% of the optical power is intentionally injected into the loop mirror by biasing the MZI to 2.91 V, the back reflections from the loop mirror become strong enough to induce instability. This is evident in the major deviations from linearity at approximately the 15-s mark or 87 mA, where an increase in drive current causes the optical power to drop significantly. The same feature occurs when decreasing drive current, indicating a repeatable feature.

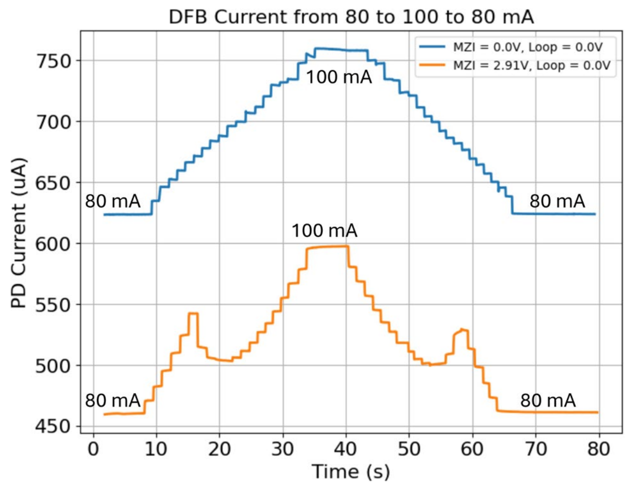

Figure 15. Output optical power vs. drive current for MZI bias at 0 and 2.91 V, respectively; the drive current was incremented manually in time by 1-mA steps approximately every second from 80 mA to 100 mA to 80 mA. The loop mirror phase shifter is held at 0 V. Significant deviations from linearity occur when sufficient light is coupled into the loop mirror, indicating unstable operation.

4.2 Back Reflections

Since parasitic back reflections induce instability in laser operation, it is useful to quantify the expected intrinsic reflections in our system. The total reflection expected in this RCC depends on routing and additional components. In our system, light that travels to a monitor PD experiences close to 10 dB loss from the 90:10 splitter, 0.5 dB from propagation loss for a single pass, and 18 dB from the PD's back reflection. Thus, the amount of light reflecting back into the laser from this path would be approximately −39 dB. For the on-chip system, only 0.5-dB loss occurs due to the 90:10 splitting ratio because more power is coupled toward that path. Propagation loss is expected to be high, at approximately 4.4 dB in one direction, due to the inclusion of a silicon modulator with higher losses. Combined with the expected PD back reflection, the round-trip loss on that branch is expected to be −28 dB. Thus, intrinsic back reflections are expected to be on the order of −28 dB at most. If the PWB loss in both travel directions is included, there is an additional −10.43 dB that further reduces this value to −38.43 dB compared with the light coming from the laser facet.

Laser stability can be predicted depending on the level of feedback and distance to the reflection using the Tkach and Chraplyvy (T-C) diagram of feedback regimes in lasers.[10] When feedback is below −45 dB, the laser may experience subtle effects from instability such as changes in linewidth or mode hops. In a narrow feedback range from approximately −45 to −39 dB, the laser is expected to be well behaved, single mode, and narrow linewidth. If feedback is higher than −39 dB, the laser will start to experience significant linewidth broadening and competing side modes. The maximum level of intrinsic back reflection we expect may place our system in the stable operation zone; if the back reflections are smaller, there may be variation in linewidth or mode hops, but any side modes will still be suppressed. As a result, the intrinsic instability in our system is expected to be minimal.

4.3 Optical Spectrum Analyzer

In our system, the RCC output only guides light to on-chip components and does not have a separate EC for monitoring the laser spectrum. To monitor the light using off-chip equipment, we placed a fiber at the reflective back end of the DFB since a small amount of light escapes and can be observed. To measure optical spectrum, the light was coupled into a Yokogawa AQ6370C OSA. As a result, the absolute power from the OSA measurements is low, but important spectral features are still evident.

The central wavelength of the laser depends on both drive current and temperature. Based on OSA measurements when the MZI and loop mirror were unheated, the laser wavelength increases with both drive current and temperature. There is some crosstalk between the two control variables, as different set points of one variable can change the slope of another. However, the wavelength can generally be predicted linearly, with an increase in wavelength of 25–30 pm/mA of drive current and 100 pm/°C (Figure 16). From this data, it is possible to tune the central lasing wavelength by a few nanometers.

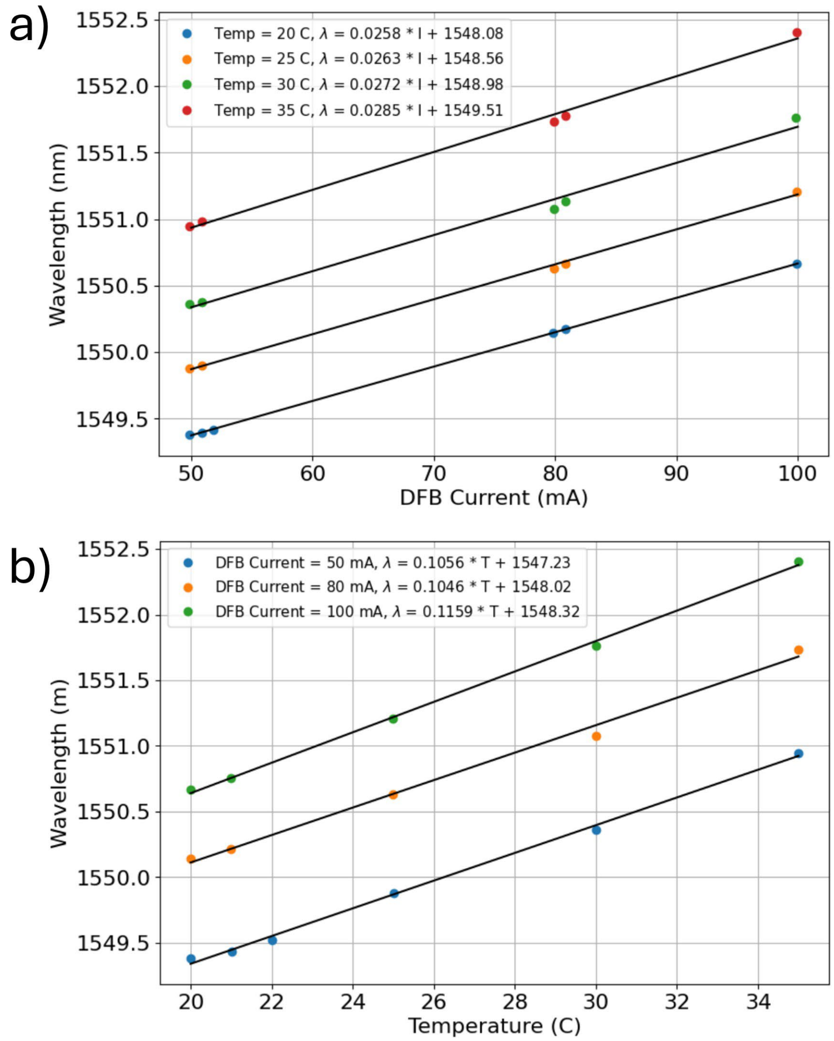

Figure 16. DFB wavelength vs. a) drive current and b) temperature at different set points.

OSA measurements can also confirm laser stability. By adjusting the MZI bias, we can control the amount of light directed toward the loop mirror and thus injected back toward the laser. For these measurements, we used the north heater in the MZI to supply bias; the south heater gave a similar result. Tuning the phase of the loop mirror can then induce or prevent instability. When the DFB is driven with 30 mA of drive current at 25 °C and the MZI is tuned from 0 to 2.5 V, less than 30% of the optical power is coupled into the loop mirror. In this regime, tuning the loop mirror from 0 to 5 V to induce a variable phase shift from 0 to π does not cause significant side modes, indicating that the laser is stable (Figure 17). Wavelength does shift depending on the loop mirror phase and may hop between modes, but the SMSR is well above 40 dB for both MZI biases, indicating that competing modes are suppressed. This measurement confirms that our PIC-laser system does not have sufficiently strong parasitic back reflections at rest to impact laser stability in a significant capacity.

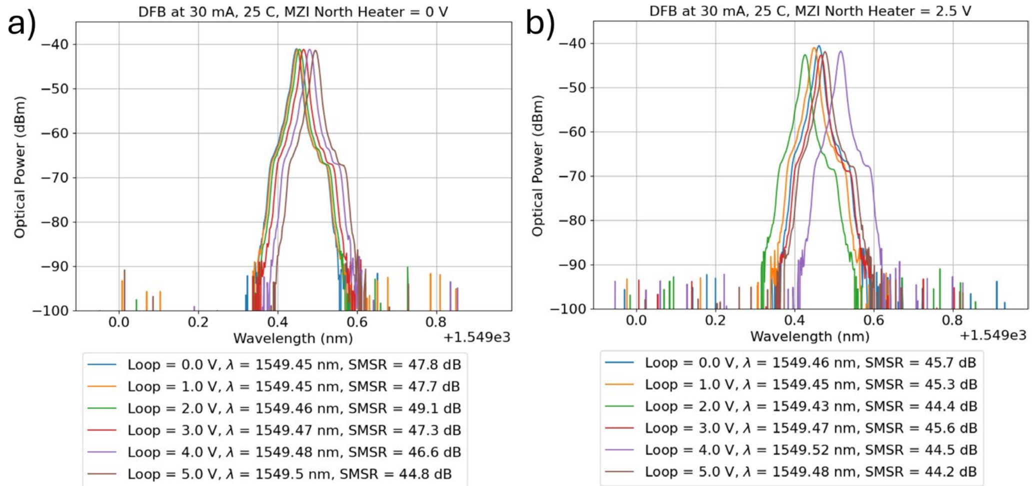

Figure 17. OSA measurements for the DFB at 30-mA drive current at 25 °C when the MZI is biased at a) 0 V, with no light directed to the loop mirror, and b) 2.5 V, directing 30% of the optical power toward the loop mirror. The phase shifter for the loop mirror is then tuned from 0 to 5 V. Both cases show high SMSR above 44 dB, indicating reasonably stable laser operation.

If the MZI is tuned from 2.91 to 4 V, more than 30% of the optical power is coupled into the loop mirror. With stronger back reflections, side modes of varying strength competitively lase depending on the phase shift applied to the loop mirror (Figure 18). The SMSR indicates the onset of these competitive modes and thus whether the laser is operating in an unstable condition. When the MZI has a 2.91 V bias, directing 30% of the light to the loop mirror, and the loop mirror is not biased, the SMSR is high at approximately 48 dB. However, the SMSR decreases to 36 and 33 dB when the loop mirror phase shifter is biased at 2 and 5 V, respectively, indicating mode competition. When the MZI is biased to 3.5 V, directing 56% of the optical power into the loop mirror, the SMSR drops to 1.3 dB at a loop mirror bias of 1 V, indicating strongly competing modes and instability. For the same MZI bias, a loop bias of 3 V recovers a SMSR of 47.5 dB, regaining stable operation. Finally, the SMSR drops as low as 0.22 dB when the MZI is biased to 4 V and loop mirror to 0 V. For the same MZI bias, the SMSR recovers to above 42 dB by changing the loop mirror bias to 1.8 V. Although our system does not have strong intrinsic instability, this mechanism of controlling phase and amplitude of back reflections can be utilized to compensate for intrinsic parasitic reflections,[5] enabling stable laser operation without resorting to an off-chip isolator. In our system, this demonstration of induced instability indicates the RCC's ability to control laser stability.

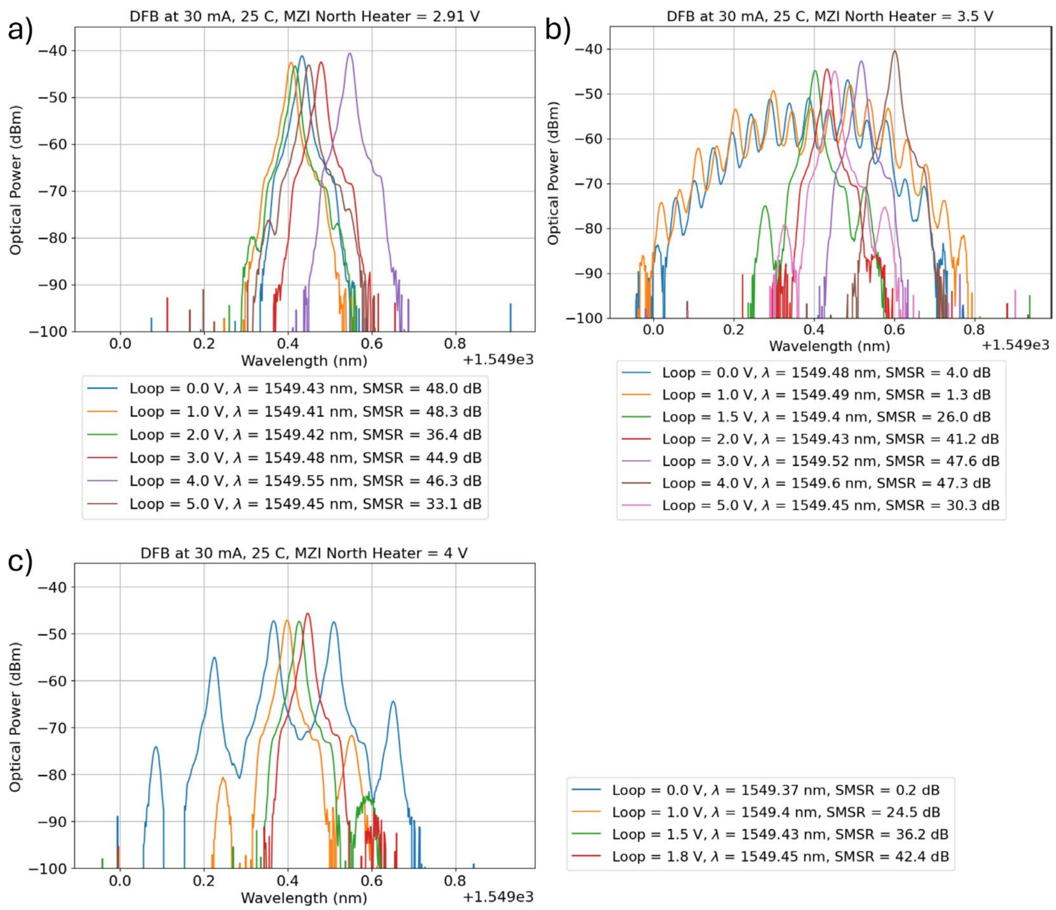

Figure 18. OSA measurements for the DFB at 30-mA drive current at 25 °C for an MZI biased at a) 2.91 V, directing 30% to the loop mirror, b) 3.5 V (56%), and c) 4 V (77%) for different loop mirror phase shifts. SMSR worsens to 35 dB or lower for at least one phase for the loop mirror, becoming as poor as 0.223 dB when the MZI is biased at 4 V and loop mirror at 0 V.

4.4 RF Power Detector

Instability can also be measured through RF noise in the photocurrent. In stable operation, RF noise is minimal, whereas unstable operation induces measurable RF noise at gigahertz frequencies. To confirm this method, we coupled light from the back end of the DFB into an external high-speed photodiode with built-in transimpedance amplifier (TIA) for amplification (Thorlabs RXM40AF, Newton, New Jersey). Its output RF signal was then monitored using a compact RF power detector (Mini-Circuits ZX47-60-S+, Brooklyn, New York) with frequency range of 10 MHz to 8 GHz. For this detector, higher RF power causes lower output voltage. Since we measured this voltage as a negative current using a 1-kΩ resistor, high RF noise indicating instability corresponds to peaks in current.

Using this method, we were able to measure stability versus both MZI bias and loop phase shifter bias for DFB drive currents at approximately 30 mA (Figure 19a) and

40 mA (Figure 19b). In both cases, we only measured significant instability when the MZI bias was 3 V or higher, directing more than 30% of the optical power toward the loop mirror. The instability onset occurred at different loop heater voltages depending on the drive current, as expected. Since these measurements were taken several weeks after the OSA measurements, there was some drift in the loop mirror bias voltages, so the unstable and stable regions occurred at different loop heater voltages between the types of measurements. However, both methods can detect laser instability. The max RF power observed was −1.4 mA = 1.4 V, which corresponds to approximately −25 to −15 dB of RF power depending on frequency according to the RF detector responsivity. Note that this detector will not detect regions of instability that induce RF noise at frequencies above 8 GHz.

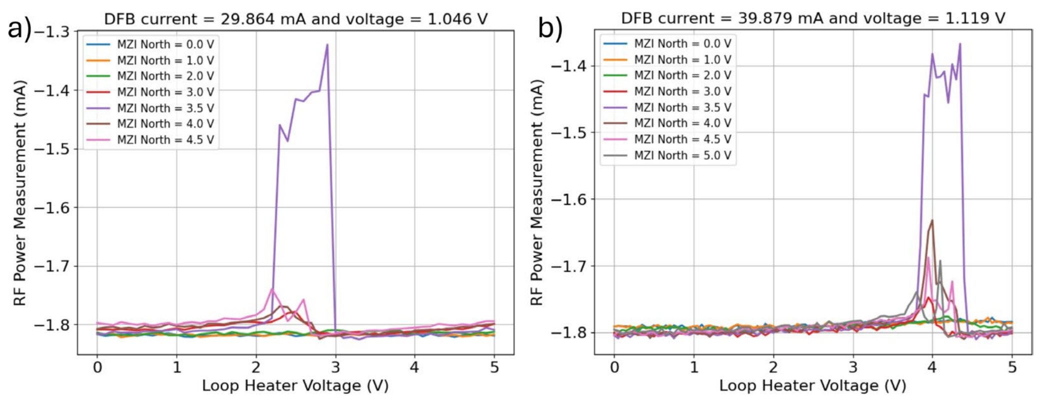

Figure 19. RF power measurements for the DFB at 25 °C for a) 30-mA and b) 40-mA drive current. Peaks in the current correspond to high RF power, indicating laser instability, and occur when the MZI bias exceeds 3 V at different loop heater biases.

4.5 RF Spectrum Analyzer

To further understand the spectrum of RF noise that is induced during unstable laser operation, we also measured RF spectra for different operation cases by connecting our external PD to an RF spectrum analyzer that operated at RF frequencies up to 26.5 GHz (Advantest R3271A). When unstable operation was induced intentionally, a fundamental peak typically appeared, along with its higher harmonics (Figure 20). Fundamental frequencies ranged from as low as 3.3 GHz to as high as 23.4 GHz, with peak powers in the −20 to −30 dB range. Note that the TIA in the external PD increased RF power, so these powers are amplified. More importantly, this measurement technique was able to pick up on a few unstable operation points that the RF power detector would not have been able to observe due to its limited frequency range.

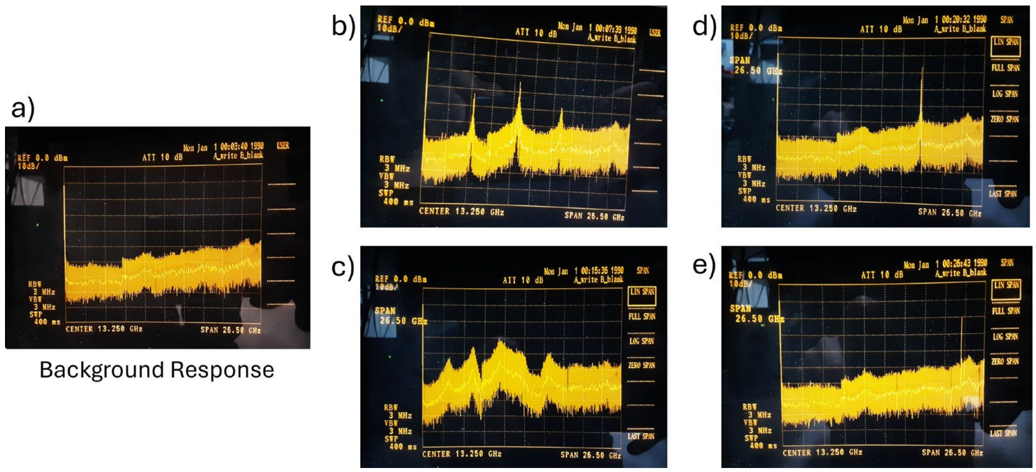

Figure 20. RF spectra measurements for the DFB at 25 °C with 30-mA drive current, using an external PD with TIA. a) Background response with the laser on; the MZI and loop heater are both at 0 V bias. b) Laser instability, with RF noise at 5.648 GHz and its harmonics, for MZI heater = 3.5 V (56% of the optical power in the loop mirror) and loop heater = 2.3 V. c) RF noise at 3.362 GHz and its harmonics, for MZI heater = 3.7 V (65% in loop) and loop heater = 2.3 V. d) RF noise at 18.351 GHz, for MZI heater = 4 V (77% in loop) and loop heater = 2.5 V. e) RF noise at 23.383 GHz, for MZI heater = 5 V (100% in loop) and loop heater = 2 V.

To confirm whether the on-chip PD can provide similar information, we used an RF probe rated up to 40 GHz (GGB 40A Picoprobe, Naples, Florida) to contact the PD pads. The probe was then connected to a high-speed bias tee with a frequency range of0.1 to 18 GHz (HP 33150A); the DC output from the bias tee was used to monitor the probe contact with the PD while the RF output was connected to the RF spectrum analyzer. To increase the RF signal strength, a +12 dB RF amplifier with operation frequency from 300 kHz to 14 GHz (Mini-Circuits ZX60-14012L-S+) was included. The RF power measured with the on-chip PD was weaker than the power measured by the external PD with TIA, ranging from −40 to −50 dB, but the RF noise response from instability was still measurable compared with the background response (Figure 21). The background response for this measurement has low-frequency noise at approximately a few gigahertz due to the amplifier. Based on Figure 21b, the on-chip PD can operate at frequencies up to 11 GHz at least, with the amplifier imposing a frequency limit below 14 GHz in this setup. Although we were able to measure unstable behavior without the amplifier (Figure 21c), the RF power was barely above the noise floor at approximately −70 dB. Thus, some form of amplification is likely necessary for practical measurements.

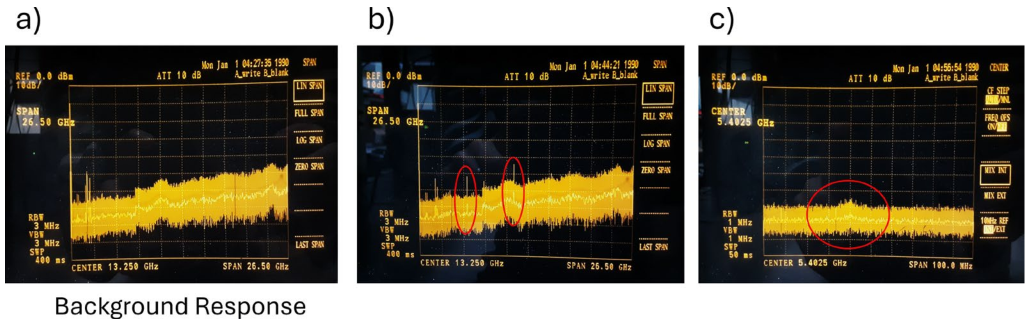

Figure 21. RF spectra measurements for the DFB at 25 °C with 30-mA drive current, using the on-chip PD, high-speed bias tee, and amplifier. a) Background response with the laser on; the MZI and loop heater are both at 0 V bias. Additional noise at lower frequencies is induced by the amplifier. b) With the amplifier, RF noise at 5.535 GHz and its next harmonic indicate instability when the MZI heater = 3.5 V (56% of the optical power in the loop mirror) and loop heater = 2.6 V. c) Zoomed-in view of 5.535 GHz peak caused by instability for the same bias point without the amplifier. The peak is barely visible above the noise floor.

5. Conclusion

We have demonstrated and characterized laser stability for a photonically wire-bonded DFB laser attached to an on-chip RCC on a PIC platform. By controlling the magnitude and phase of back reflections using on-chip structures, the laser can be forced into a stable or unstable operating state. Although our current system has minimal intrinsic back reflections, improvements to PWB loss or including output ECs in the PIC system may increase intrinsic back reflections enough to induce instability in the attached laser. In these future designs, the RCC will become a necessity for controlling laser stability. Future iterations of these experiments will also explore more compact methods to monitor and avoid instability, such as using off-chip envelope detectors or on-chip electronics to measure RF noise. By providing quantitative feedback on laser stability, we will ultimately be able to automate control of the RCC and ensure stable laser operation in a variety of PIC-based applications that utilize attached lasers.

6. References

1. Huang D, Pintus P, Bowers JE. Towards heterogeneous integration of optical isolators and circulators with lasers on silicon [invited]. Opt Mater Express. 2018;8(9):2471–2483. https://doi.org/10.1364/OME.8.002471

2. Tian H et al. Magnetic-free silicon nitride integrated optical isolator. Nat Photon. 2021;(15):828–836. https://doi.org/10.1038/s41566-021-00882-z

3. White AD et al. Integrated passive nonlinear optical isolators. Nat Photon. 2022;(17):143–149. https://doi.org/10.1038/s41566-022-01110-y

4. Xiang C et al. 3D integration enables ultralow-noise isolator-free lasers in silicon photonics. Nature. 2023;(620):78–85. https://doi.org/10.1038/s41586-023-06251-w

5. Esmaeeli O, Chrostowski L, Shekhar S. Isolator-free laser operation enabled by chip-scale reflections in zero-process-change silicon-on-insulator. Nat Photon. 2026;20(332–339). https://doi.org/10.1038/s41566-026-01850-1

6. Yoshioka VJ, Cho PS, Bickford JR. Mitigation of intrusive higher order modes in photonic integrated circuits. Opt Exp. 2026;34(17):31691–31706. https://doi.org/10.1364/OE.605495

7. Hu X et al. High-speed and high-power germanium photodetector with a lateral silicon nitride waveguide. Photon Res. 2021;9(5):749–756. https://doi.org/10.1364/PRJ.417601

8. Byrd MJ et al. Mode-evolution-based coupler for high saturation power Ge-on-Si photodetectors. Opt Lett. 2017;42(4):851–854. https://doi.org/10.1364/OL. 42.000851

9. Ghannam I, Merget F, Witzens J. Silicon nitride C-band grating couplers with reduced waveguide back-reflection. In: Chen RT, Schröder H, editors. Optical interconnects xxii. SPIE; 2022. p. 120070N. https://doi.org/10.1117/12.2607729

10. Donati S, Horng R-H. The diagram of feedback regimes revisited. IEEE J Sel Top Quantum Electron. 2013;19(4):1500309–1500309. https://doi.org/10.1109/JSTQE.2012.2234445

List of Symbols, Abbreviations, and Acronyms

3D	Three-Dimensional
AOI	Applied Optoelectronics, Inc.
ARL	Army Research Laboratory
DC	Directional Coupler
DEVCOM	U.S. Army Combat Capabilities Development Command
DFB	Distributed Feedback
EC	Edge Coupler
HOM	Higher-Order Mode
HOMB	HOM Block
MFD	Mode Field Diameter
MMI	Multi-Mode Interferometer
MZI	Mach-Zehnder Interferometer
OSA	Optical Spectrum Analyzer
PD	Photodetector
PIC	Photonic Integrated Circuit
PWB	Photonic Wire Bond
RCC	Reflection Controlling Circuit
RF	Radio Frequency
SMSR	Side Mode Suppression Ratio
T-C	Tkach and Chraplyvy
TIA	Transimpedance Amplifier

1 (PDF)	DEFENSE TECHNICAL INFORMATION CTR DTIC OCA
1 (PDF)	DEVCOM ARL FCDD RLB CB TECH LIB